



# **JGR** Atmospheres

### **RESEARCH ARTICLE**

10.1029/2023JD039972

### **Key Points:**

- Mean precipitation and hail frequency are higher downwind of Dallas-Fort Worth except on the wettest days
- Deep convection properties do not respond linearly to urban extent
- Microphysical schemes affect the sign of response in metrics of deep convection to urban extent

### **Supporting Information:**

Supporting Information may be found in the online version of this article.

#### Correspondence to:

X. Zhou, xin.zhou@cornell.edu

### Citation:

Zhou, X., Letson, F., Crippa, P., & Pryor, S. C. (2024). Urban effect on precipitation and deep convective systems over DallasFort Worth, Journal of Geophysical Research: Atmospheres, 129. e2023JD039972. https://doi.org/10.1029/ 2023JD039972

Received 8 SEP 2023 Accepted 21 APR 2024

### **Author Contributions:**

Conceptualization: Xin Zhou, Sara C. Pryor

Formal analysis: Xin Zhou, Fred Letson Funding

acquisition: Paola Crippa, Sara

Investigation: Xin Zhou, Fred Letson Methodology: Xin Zhou, Fred Letson, Sara C. Prvor

Resources: Sara C. Pryor Supervision: Sara C. Pryor Validation: Xin Zhou, Fred Letson.

Paola Crippa, Sara C. Pryor

Visualization: Xin Zhou, Fred Letson Writing - original draft: Xin Zhou, Fred

Letson, Sara C. Pryor

Writing - review & editing: Xin Zhou. Fred Letson, Paola Crippa, Sara C. Pryor

# **Urban Effect on Precipitation and Deep Convective Systems Over Dallas-Fort Worth**

Xin Zhou<sup>1</sup>, Fred Letson<sup>1</sup>, Paola Crippa<sup>2</sup>, and Sara C. Pryor<sup>1</sup>

<sup>1</sup>Department of Earth and Atmospheric Sciences, Cornell University, Ithaca, NY, USA, <sup>2</sup>Department of Civil and Environmental Engineering and Earth Sciences, University of Notre Dame, South Bend, IN, USA

Abstract A range of multi-year observational data sets are used to characterize the hydroclimate of the Dallas Fort-Worth area (DFW) and to investigate the impact of urban land cover on daily accumulated precipitation, RADAR composite reflectivity (cREF), and cloud top height (CTH) during the warm season. Analyses of observational data indicate rainfall rates (RR) in a 45° annulus sector 50-100 km downwind of the city are enhanced relative to an upwind area of comparable size. Enhancement of mean precipitation intensity in this annulus sector is not observed on days with spatially averaged RR > 6 mm/day. Under some flow directions, the probability of cREF >30 dBZ, occurrence of hail, and the probability of CTH >10,000 geopotential meters are also enhanced up to 200 km downwind of DFW. Two deep convection events that passed over DFW are simulated with the Weather Research and Forecasting model using a range of microphysical schemes and evaluated using RADAR observations. Model configurations that exhibit the highest fidelity in these control simulations are used in a series of perturbation experiments where the areal extent of the city is varied between zero (replacement with grassland) and eight times its current size. These perturbation experiments indicate a non-linear response of Mesoscale Convective System properties to the urban areal extent and a very strong sensitivity to the microphysical scheme used. The impact on precipitation from the urban area, even when it is expanded to eight-times the current extent, is much less marked for deep convection with stronger synoptic forcing.

Plain Language Summary Urban areas are rapidly expanding and have the potential to strongly influence the local and regional climate. Long-term warm season observations near Dallas-Fort Worth show

## 1. Introduction

Urban areas profoundly influence the atmosphere and may alter precipitation regimes (Bornstein & Lin, 2000; Dixon & Mote, 2003; Oke et al., 2017; Qian et al., 2022; Rosenzweig et al., 2018; Shepherd et al., 2002; USGCRP,

- 1. Modification of thermal and moisture regimes via changes in the surface energy balance (e.g., development of the urban heat island, UHI) and the induced changes in circulation patterns over and downwind the urban
- 2. Modification of dynamical processes due to the enhanced urban roughness length and resulting changes in circulation patterns over the urban area relative to the regional flow.
- 3. Modification of cloud microphysics due to urban emissions of aerosols and precursor gases.

These mechanisms do not act in isolation. For example, the presence of a strong UHI can initiate convective activity and enhance precipitation over the city (USGCRP, 2017). Conversely, strong winds and weak UHI may cause thunderstorms to bifurcate and move around cities because of building barrier-effects (Dou et al., 2015). This may lead to maximum precipitation occurring around the city in lateral boundary convergence zones and in the downwind reconvergence area, while the minimum precipitation occurs over and downwind cities (Rosenfeld et al., 2008). Once convection is initiated, urban enhancement of atmospheric aerosols can also influence the dynamics, microphysics, and precipitation produced by convective storms (Rosenfeld et al., 2008).

Reserved.

© 2024. American Geophysical Union. All Rights Nevertheless, simulations of a severe convective storm that impacted Kansas City found the combination of chemical and

ZHOU ET AL. 1 of 22



# Journal of Geophysical Research: Atmospheres

10.1029/2023JD039972

higher rainfall intensity and hail frequency 50–100 km downwind of the city, but those days with the heaviest precipitation are not enhanced by the city. Numerical simulations show that atmospheric responses to urbanization are very sensitive to the precise model configuration used which means there are still large uncertainties in projecting how urbanization may influence atmospheric hazards. physical forcing increased the probability of occurrence of hail stones >1 inch by  $\sim$ 20% which is greater than the influence from any individual process (Yun Lin et al., 2021).

One of the first studies to report an urban influence on precipitation focused on La Porte (~80 km downwind from Chicago) where a warm season spatial anomaly of +33% in precipitation amounts was reported during 1929- 1963 (Changnon Jr, 1968). Attribution of this anomaly prompted considerable controversy and was hampered by measurement limitations/uncertainties (Changnon Jr, 1968, 1980; Clark, 1979; Holzman & Thom, 1970). Results from the METROpolitan Meteorological EXperiment (METROMEX) suggested "statistically significant increases in summer rainfall, heavy (>2.5 cm) rainstorms, thunderstorms and hail in and just east (downwind) of St. Louis" compared to upwind regions (Changnon Jr, 2016; Changnon Jr et al., 1976). Additional observational studies have also generally found higher precipitation over and downwind of major US urban areas than upwind particularly during the warm season (Dixon & Mote, 2003; Hand & Shepherd, 2009; Huff & Changnon, 1973; McLeod & Shepherd, 2022; McLeod et al., 2017; Shepherd & Burian, 2003; Shepherd et al., 2002). Analyses focused on Houston in the US Southern Great Plains (SGP) found the urban area and downwind regions exhibit enhancement of warm season afternoon precipitation by 59% and 30%, relative to upwind regions (Burian & Shepherd, 2005). Analyses of data from RADAR and rain gauges found enhanced warm season precipitation 15- 70 km downwind of New York City and Milwaukee, although elevation effects greatly confounded quantitative assessment around New York City and the spatial gradients of precipitation were only partly resolved in numerical simulations (Keuser, 2014; Yeung et al., 2015; Yeung et al., 2011). Enhanced summer-season cloud-toground lightning flash density downwind of Houston (Gauthier et al., 2006) and other cities (Burke & Shepherd, 2023) has been attributed to enhanced convection over urban areas. Further evidence of an urbanization signal in enhancement of heavy rainfall 50 km downwind of cities was found based on an analysis of 50-year data from 4,593 surface stations (Niyogi et al., 2017). A meta-analysis of global studies suggested mean rainfall rates are increased by an average of 16% over the urban center and 18% at an average distance of 20-50 km downwind of urban areas relative to upwind regions (Liu & Niyogi, 2019). An increased probability of occurrence of daily precipitation of 100-200 mm over time was also reported in rain-gauge observations downwind of Beijing during the monsoon season (Hu, 2015; Y Zhang et al., 2014).

Numerical simulations reveal complex responses of the hydroclimate to urbanization and urban surface with different combinations of UHI, surface roughness length, aerosol concentration, urban size, location, and precipitating systems (Han et al., 2014; Kusaka et al., 2014; Lauer et al., 2023; Li et al., 2021; Shepherd et al., 2010; Wang et al., 2018; J Zhang et al., 2020; Zhong et al., 2015). An ensemble of simulations over Tokyo found an increase in precipitation over the metropolitan area due to enhanced UHI which destabilized the atmosphere and induced moisture convergence in a moisture-rich environment near the coast (Kusaka et al., 2014). Conversely, simulations over Beijing found the reduction in evapotranspiration of the city due to the increased impermeable surface led to a net decrease in summer precipitation (Wang et al., 2018). Another numerical study in the Beijing-Tianjin-Hebei region found a non-linear response in heavy precipitation due to urbanization; The UHI was found to increase hourly precipitation over the urban and downwind regions in the early stage of urbanization but further urban expansion reduced precipitation due to reduced evaporation (J Zhang et al., 2020). A year-long simulation over the Guangdong-Hong Kong-Macau area found an increased extreme convective precipitation with urbanization due to increased surface roughness length, enhanced low-level convergence, and enhanced sensible heat flux from the UHI, but the urban surface has little effect on extreme precipitation associated with frontal and Typhon systems that are associated with stronger large-scale forcing (Li et al., 2021). The dependence of an urban rainfall effect on the synoptic environment is also indicated by other studies (Debbage & Shepherd, 2019; Lauer et al., 2023; McLeod & Shepherd, 2022), with weaker precipitation impacts under largescale synoptic systems (Lauer et al., 2023). Consistent with observational studies, most numerical studies show any hydroclimatic response to urban land use is most pronounced within about 100 km of the city center, but the location and effect vary between studies. Shem and Shepherd (2009)

ZHOU ET AL. 2 of 22

wiley.com/doi/10.1029/2023JD039972 by Cornell University Library, Wiley Online Library on [29/07/2024]. See the Terms and Condit

found increased precipitation 20–50 km downwind of the city, while Wang et al. (2018) found decreased precipitation  $\sim$ 100 km upwind of major city with extensive urbanization.

Multiple previous studies have demonstrated a strong dependence of simulated deep convection on the microphysical scheme applied. For example, Fan et al. (2017) performed WRF simulations of a mesoscale squall line with eight different microphysical schemes and found substantial differences in simulated precipitation and that use of a spectral-bin microphysical scheme did not enhance model fidelity. Although a dependence of urbanatmosphere feedbacks on model parameterizations (including microphysical scheme) has been previously

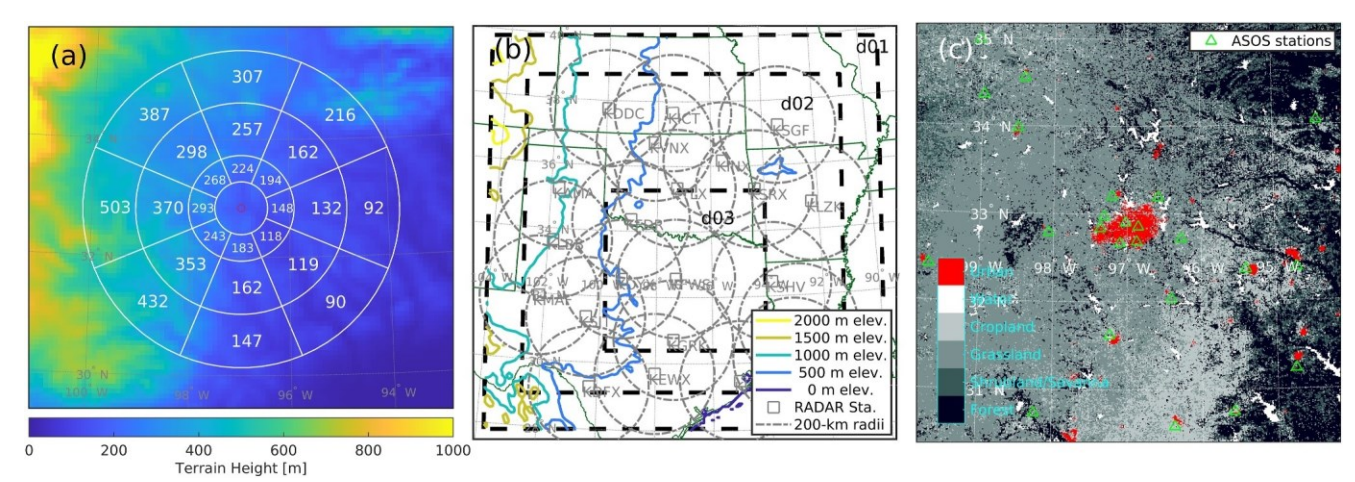


Figure 1. Southern Great Plains study domain. (a) Terrain elevation (a.s.l.) around Dallas Forth Worth (DFW) and mean terrain elevation in 45° direction sectors in three range bands (i.e., distances from the center of DFW): 50–100 km, 100–200 km, and 200–300 km. (b) The three WRF domains (areal extent of domain three is as shown in frame (a)), with the locations of NWS dual-polarization Doppler RADAR and 200 km radii from which data are reported (gray) and topography. State borders are shown in dark green. (c) Domain 3 Land Use/Land Cover classes and the location of NWS ASOS surface observing stations.

reported (Yu et al., 2018), relatively few previous studies have included different microphysical schemes in urban land cover perturbation experiments.

Here we further examine the issue of urban impacts on precipitation and deep convection using a combination of (a) analyses of long-term observational data sets and (b) targeted WRF simulations. In the simulations, we focus on the impact of land cover and thus mechanisms 1 and 2 listed above without aerosol effects due to the large uncertainties associated with aerosol forcing. Our study domain is focused on Dallas-Fort Worth (DFW, Figure 1) because it is an isolated large metropolis located in the US Southern Great Plains, a region with frequent deep convection associated with mesoscale convective systems (MCS) during the March to September warm season (Feng et al., 2019; Feng et al., 2021; Fritsch et al., 1986; Pryor et al., 2023). Beyond precipitation amounts here we also diagnose urban impacts on hail production and maximum hail diameter because it is a societally relevant component of extreme hydrometeorology (Prein & Holland, 2018; Punge & Kunz, 2016) and severe hail occurs on approximately 5% of days in the SGP (Prein & Holland, 2018; Trapp et al., 2019). Our specific objectives are as follows.

- 1. Quantify the influence of DFW on the observed precipitation climate and whether the presence of an urban signature exhibits a dependence on precipitation intensity and spatial scale.
- 2. Quantify the fidelity of high-resolution simulations with WRF for deep convection events; Examine (a) the dependence of any urban influence on model configuration and urban area expanse and (b) the degree to which any impact is consistent across events with different large-scale forcing. Note that the surface energy balance and roughness length generally have a larger impact on convective intensity and hail production than aerosols herein, we primarily focus on non-aerosol effects. Nevertheless, in light of evidence that the impact of urban aerosols on downwind storms decreases with increasing background aerosol concentrations (Van

ZHOU ET AL. 3 of 22

Den Heever & Cotton, 2007), additional experiment is performed to examine the sensitivity of the simulations to different cloud droplet number concentrations (Nc) used in the Morrison microphysical scheme.

### 2. Materials and Methods

## 2.1. Observational Data Sets

In situ heated, tipping bucket rain gauge data for 2005–2021 from 10 National Weather Service (NWS) Automated Surface Observing Stations (ASOS) (Nadolski, 1998) closest to DFW are used to describe the precipitation climatology. Seven are within 50 km and nine are within 100 km of the DFW centroid. The spatially heterogeneous distribution of the ASOS network precludes its use in analyses of potential urban enhancement of precipitation. The primary data set used for that purpose is the Stage IV NCEP/EMC product (Du, 2011). It is derived by integration of data from NWS RADAR and rain gauges and is available hourly with 4 km spatial resolution across the contiguous USA (Ying Lin & Mitchell, 2005; Nelson et al., 2016). Stage IV has been used as a target data set for the evaluation of numerical model output and other precipitation data products (Beck et al., 2019; Pryor et al., 2023; Smalley et al., 2014). Herein, spatial fields of daily accumulated precipitation (from 00Z) at 4-km resolution over the period 2002–2021 are conditionally sampled by wind direction as characterized using the ERA5 reanalysis product (Hersbach et al., 2020) (see below).

Analyses presented here also include cloud top height (CTH) estimates from Advanced Baseline Imager channels on the National Oceanic and Atmospheric Administration GOES-16 satellite from 2018 to 2021 (Heidinger et al., 2020; Schmit et al., 2005). CTH from GOES-16 is reported at a 2-km spatial resolution every five minutes (Khlopenkov et al., 2021). Daily maximum CTH in each grid cell is conditionally sampled by ERA5 wind direction to evaluate whether there is evidence that the DFW conurbation induces higher topped clouds and by association enhancement/suppression of deep convection.

Data collected by NWS WSR-88D dual-polarization Doppler RADAR (Crum et al., 1998; Seo et al., 2015) during two deep convection events are used herein to direct and evaluate the WRF simulations. The long-term analyses focus on data from KFWS (Dallas-Fort Worth; 32.5728°N 97.3031°W). These RADAR perform 360° azimuth scans at between nine and 14 elevation angles (0.5°-19.5°) every 5-10 min depending on precipitation conditions (NOAA, 2016a, 2017). Data are archived with an azimuthal resolution of 1° and range resolution of 0.25 km. Four RADAR-derived properties are used herein; composite reflectivity (cREF, dBZ), precipitation rate (mm/h) (NOAA, 2016a), Hybrid Hydrometeor Classification (HHC) (Chandrasekar et al., 2013; NOAA, 2016b) and storm/hail reports. In the climatological analyses we use the frequency of occurrence of daily maximum cREF >30 dBZ, as a metric of the presence of convection (Pryor et al., 2023; Stolz et al., 2015; Xu et al., 2017). WSR88D RADAR algorithms track convective cells within each RADAR's scanned area and also estimate CTH, hail probability and maximum hail size (Crum et al., 1998; NOAA, 2016b; Seo et al., 2015; Wallace et al., 2019; Witt et al., 1998). The frequency of hail and graupel reports in the HHC data is strongly influenced by distance from the RADAR, because the elevations scanned by the RADAR increase with range, and some parts of the cloud may be unsampled at short or long range. Thus, the probability of hail and graupel is reported for 150 and 200 km distances from KFWS. RADAR data are regridded onto the WRF grid by inverse-distance averaging when used in WRF evaluation.

## 2.2. Analyses of Observational Data

A daily mean wind direction at 850 hPa is used to describe advection following past research (Niyogi et al., 2017) and is derived by averaging the hourly u and v wind components from the ERA5 reanalysis over the grid cells around DFW. In the climatological analyses all atmospheric properties are conditionally sampled by daily mean wind direction in eight, 45° directional sectors (Figure 1a). As an example, a quantitative assessment of possible urban intensification of precipitation is produced by quantifying and comparing Stage IV daily rainfall totals in 45° annulus sectors at a range of 50–100 km upwind (UW) and downwind (DW) of DFW (Figure 1a). For each day, spatially averaged daily total precipitation is computed in these upwind and downwind annulus sectors

ZHOU ET AL. 4 of 22

com/doi/10.1029/2023JD039972 by Cornell University Library, Wiley Online Library

along with the 50th, 60th, 70th, 80th, and 90th, percentile values in all grid cells within each annulus sector. For days with non-zero precipitation in both the upwind and downwind sectors, the ratio of the percentiles in the DW to UW sectors is used to assess the differential effect of the presence of DFW on lighter and heavier precipitation. A non-parametric Mann-Whitney (Wilcoxon Rank Sum) test is used to assess the statistical significance of differences in the median values of precipitation samples upwind and downwind of DFW (Wilks, 2011).

Past research has demonstrated a differential urban impact on precipitation dependent on the synoptic forcing. Thus, the mean-minimum distance (MMD) is used as a metric of the spatial scale of precipitation for days with mean Stage IV daily precipitation upwind of DFW >6 mm. The MMD is the mean shortest axis of contiguous areas of Stage IV grid cells with total daily precipitation >2 mm. Larger MMD is interpreted as precipitation events with larger-scale forcing and thus are less likely to be influenced by the urban area.

#### 2.3. WRF Simulations

Two MCS events that passed over DFW are simulated with WRF v4.3 (Skamarock et al., 2019). Both are intense convective systems that occurred during the warm season of 2017 and were selected to represent two different types of deep convection: (a) March 29 typifies springtime MCS events associated with large-scale circulation and baroclinic forcing (Feng et al., 2019). It has a relatively high MMD and was associated with a low-pressure system and strong convergence near the surface with strong upper-level divergence and a deep trough to the west, resulting in high rainfall totals from both widespread deep convection and stratiform precipitation; (b) July 4 is more typical of events with weaker baroclinic forcing (Feng et al., 2019) and has a smaller MMD. The environmental context was dominated by a high-pressure system with weak low-level convergence acting on the warm, humid air associated with weak pressure gradient. Both event days exhibit relatively widespread high composite reflectivity and heavy precipitation. The mean daily total precipitation within 200 km of DFW are 15.6 and 16.1 mm respectively, which are both greater than 89% of warm-season days, according to Stage IV data. Daily precipitation totals exceeded 6 mm in 98.4% and 82.7% of Stage IV cells within 200 km of DFW on March 29 and July 4, respectively. Hail and graupel occurred near DFW during both events. Up to 21% of grid cells within 150 km of DFW exhibited hail (1%) or graupel (20%) during 29 March 2017, and 11% exhibited hail or graupel during 4 July 2017 (Figure S1 in Supporting Information S1). The maximum estimated hail size (MESH) within 100 km of DFW for each event was 38.2 mm. Deep convection close to DFW was most evident at 07:20 UTC on March 29 and 06:40 UTC on July 4 (SI Figure S1 in Supporting Information S1).

WRF is first used to perform an ensemble of control (CTL) simulations of each event using five microphysical schemes: Milbrandt-Yau (MILB (Milbrandt & Yau, 2005)), Morrison (MORR (H. Morrison et al., 2009)), Thompson aerosol aware (THOMA (Thompson & Eidhammer, 2014)), WRF double moment seven categories (WDM7 (Bae et al., 2018)), and NSSL (Mansell et al., 2010). All have relatively sophisticated representations of frozen hydrometers and are double-moment in cloud water except for MORR. To make the microphysical schemes more comparable in the control simulations, a typical continental aerosol number concentration of 300 cm<sup>-3</sup> is used for all schemes that consider cloud droplet activation, while the default fixed Nc of 250 cm<sup>-3</sup> for continental contexts is used for MORR assuming most of the aerosol would be activated. To examine the sensitivity of the urban precipitation response to Nc, an additional experiment is also performed where Nc is set to 350 cm<sup>-3</sup>. Note that the MORR scheme does not distinguish hail from graupel. To capture the hail properties, we use the hail density for the graupel + hail category of MORR scheme by enabling the namelist option "morr rimed ice". Other model settings include the Mellor-Yamada-Nakanishi-Niino level 2.5 (MYNN) planetary boundary layer (PBL) scheme (Nakanishi & Niino, 2006) with the eddy diffusivity/mass flux (EDMF) option turned on to better simulate shallow convections. The scale-aware Grell-Freitas scheme (Grell & Freitas, 2014) is used to parameterize deep convection in the parent domain (d01). The Noah land surface model (F Chen & Dudhia, 2001; F Chen et al., 1996; Tewari et al., 2004) is used along with the longwave (LW) and shortwave (SW) Rapid Radiative Transfer Models for General Circulation Model application (RRTMG (Iacono et al., 2008)). Each simulation lasts 36 hr starting at 1200 UTC on the previous day with the first 6 hr treated as spin-up. In initial

ZHOU ET AL. 5 of 22



testing two sets of lateral and initial boundary conditions were selected; ERA5 and the High Resolution Rapid Refresh (HRRR) analysis. Given the relatively coarse resolution of ERA5 (~30 km), three nested domains (Figure 1b) with 66 vertical levels are used at grid spacings of 9, 3, and 1 km, respectively. The initial testing demonstrated a clear superiority of the HRRR and thus only results from those simulations are presented here.

## 2.4. Analyses of WRF Output and Perturbation Experiments

The CTL simulations are evaluated for a range of properties during time intervals centered on the passage of the convection over DFW  $(t_p)$  using the metrics summarized on Taylor diagrams (Taylor, 2001); root mean square error, correlation coefficients, and relative field variability (ratio of standard deviations). We also compute the relative Euclidean distance (D) (Wu et al., 2012) which considers all three aforementioned aspects at once (SI Eq 1 in Supporting Information S1).

We perform four perturbation experiments in which the size of DFW is altered while maintaining the water grids and urban morphology. In the first experiment, DFW is replaced by the most commonly occurring non-urban land use in the domain - grassland (DFW  $\times$  0). The urban land cover is then expanded to twice (DFW  $\times$  2), fourtimes (DFW  $\times$  4), and eight-times (DFW  $\times$  8) the current area. This range includes a population-based projection for a tripling of DFW by the end of 21st century under a high urban expansion scenario (Gao & Bukovsky, 2023). Nevertheless, the projected urban expansion and corresponding urban effect are relatively small compared to the deep convective systems simulated. Therefore, we use a range of urban enhancements up to DFW  $\times$  8 to better extract urban effect from other factors. These perturbations are applied by changing the land use category and land use fraction in the WRF Preprocessing System (WPS) generated "met\_em" files before producing the initial and boundary conditions.

To characterize the urban influence only on precipitating regions of the deep convective systems, we apply an MCS tracking algorithm based on the brightness temperature (Elsaesser et al., 2022; Fiolleau & Roca, 2013) and further include only grid cells with cREF >20 dBZ, which is a threshold at which precipitation typically begins (Matyas, 2007). The feature tracking algorithm and MCS-scale-averaged properties provide an easy way to identify the upwind and downwind areas regardless of the precise moving direction of the MCSs as long as the time of convection passage over DFW,  $t_p$ , is identified.

# 3. Hydroclimate of the DFW Area and Analyses of the Urban Signature From Observations

Annual mean rainfall from the 10 ASOS stations (2005–2021) ranges from 700 to 1,100 mm. Across those stations, rainfall rates (RR) > 0 mm/hr are reported in 2.43%–3.09% of all 5-min periods, and RR > 4 mm/hr occurs in 0.98%–1.30% of 5-min periods. Probabilities of RR > 25 mm/hr and >50 mm/hr are 0.15%–0.21% and 0.050%–0.085%, respectively. Stage IV daily precipitation totals (2002–2021) > 0 mm in at least one Stage IV grid cell within 50 km of the DFW centroid on 49% of warm-season days. Daily precipitation totals in at least one of these Stage IV grid cells exceed 25 and 50 mm in 8.6% and 1.9% of all warm-season days, respectively.

Spatial fields of warm-season mean daily total precipitation and the number of days with daily precipitation >5 mm from Stage IV, when conditionally sampled by wind direction, indicate higher values downwind of DFW for westerly and southwesterly flow (Figure 2). For southwesterly flow, 12% of Stage IV grid cells within WRF domain d03 have daily precipitation >5 mm on >20% of days. All these grid cells are downwind of DFW. For westerly flow, 30% of Stage IV grid cells in domain d03 have >5 mm of daily precipitation on >20% of days. Again, all are downwind of DFW. There is also evidence that daily precipitation totals are higher downwind of DFW under southerly flow, though daily totals above 5 mm are considerably less frequent under other flow conditions (Figure 2g). The areas with enhanced precipitation tend to be focused about 50–200 km downwind (and beyond), which overlaps the range of distances at which downwind effects have been detected in previous work; 16–80 km in Huff and Changnon Jr (1973) and 50–150 km in Shepherd and Burian (2003).

ZHOU ET AL. 6 of 22



# Journal of Geophysical Research: Atmospheres

10.1029/2023JD039972

Daily grid-cell rainfall totals were conditionally sampled within three classes of mean rainfall in the upwind sector ( $R_{mean}$ ):  $0 < R_{mean} < 1$  mm,  $1 < R_{mean} < 6$  mm, and  $R_{mean} > 6$  mm. The spatial median values in the downwind sector are higher than those in the upwind sector according to the Wilcoxon rank-sum test when  $R_{mean}$  is low (i.e., for  $0 < R_{mean} < 1$  mm and  $1 < R_{mean} < 6$  mm). For days with upwind  $R_{mean} > 6$  mm (i.e., the top 25% of wet days), this test indicates significantly lower spatial median rainfall totals downwind of DFW. The upwind sample of grid-cell mean daily total precipitation also contains a higher frequency of values below 4 mm than those sampled downwind. Further, on a typical day, the 50th, 60th, 70th, 80th, and 90th percentile daily precipitation totals in the downwind sector, sampled in space, are higher than those in the upwind sector and the enhancement is similar across different percentile values (SI Figure S2 in Supporting Information S1). On average the grid cells that represent the  $N^{th}$  percentile of precipitation totals in the downwind sector receive about 1.4 times as much precipitation as those in the upwind sector. Thus, the downwind sector is more likely to include locations with more intense precipitation.

Upwind-downwind differences in daily precipitation totals are also a strong function of MMD. Larger-scale events (MMD > 100 km) are more often associated with lower precipitation downwind of DFW, while smaller (MMD < 100 km), locally forced events are more likely to show statistically significant enhancement of precipitation in the downwind sector (Table 1). The two events chosen for WRF simulation herein are both in the highest  $R_{mean}$  category ( $R_{mean} > 6$  mm), but exhibit different MMD. The March event has an MMD of 200 km (the 97th percentile of MMD for all warm season days with  $R_{mean} > 6$  mm), represents events that, on average, exhibit upwind enhancement of precipitation. The July event is characterized by an MMD of 85 km and represents events that have a higher probability of exhibiting downwind enhancement of precipitation (Table 1).

Maximum daily cREF >30 dBZ is more frequently observed downwind of DFW than upwind of the city (Figure 3). Maximum daily cREF >30 dBZ occurs on more than 35% of days with westerly, southwesterly and southerly flow in many areas >100 km downwind of DFW, but has a probability of <0.3 in comparable upwind regions. Within 100 km of DFW, high cREF is also more common downwind than upwind for these wind directions. The mean frequency of daily maximum cREF >30 dBZ sampled across all RADAR grid cells is 29%—45% higher in downwind 45° annulus sectors 50–100 km from DFW than upwind of the city for westerly, southwesterly and southerly flow (Figure 3). No difference is found for other wind directions. The probability of

ZHOU ET AL. 7 of 22

21698996, 2024, 10, Downloaded from https://agupubs.onlinelibrary.wiley.com/doi/10.1029/2031/D039972 by Cornell University Library, Wiley Online Library on [29/07/2024]. See the Terms and Conditions (https://onlinelibrary.wiley.com/terms-and-conditions) on Wiley Online Library for rules of use; OA articles are;

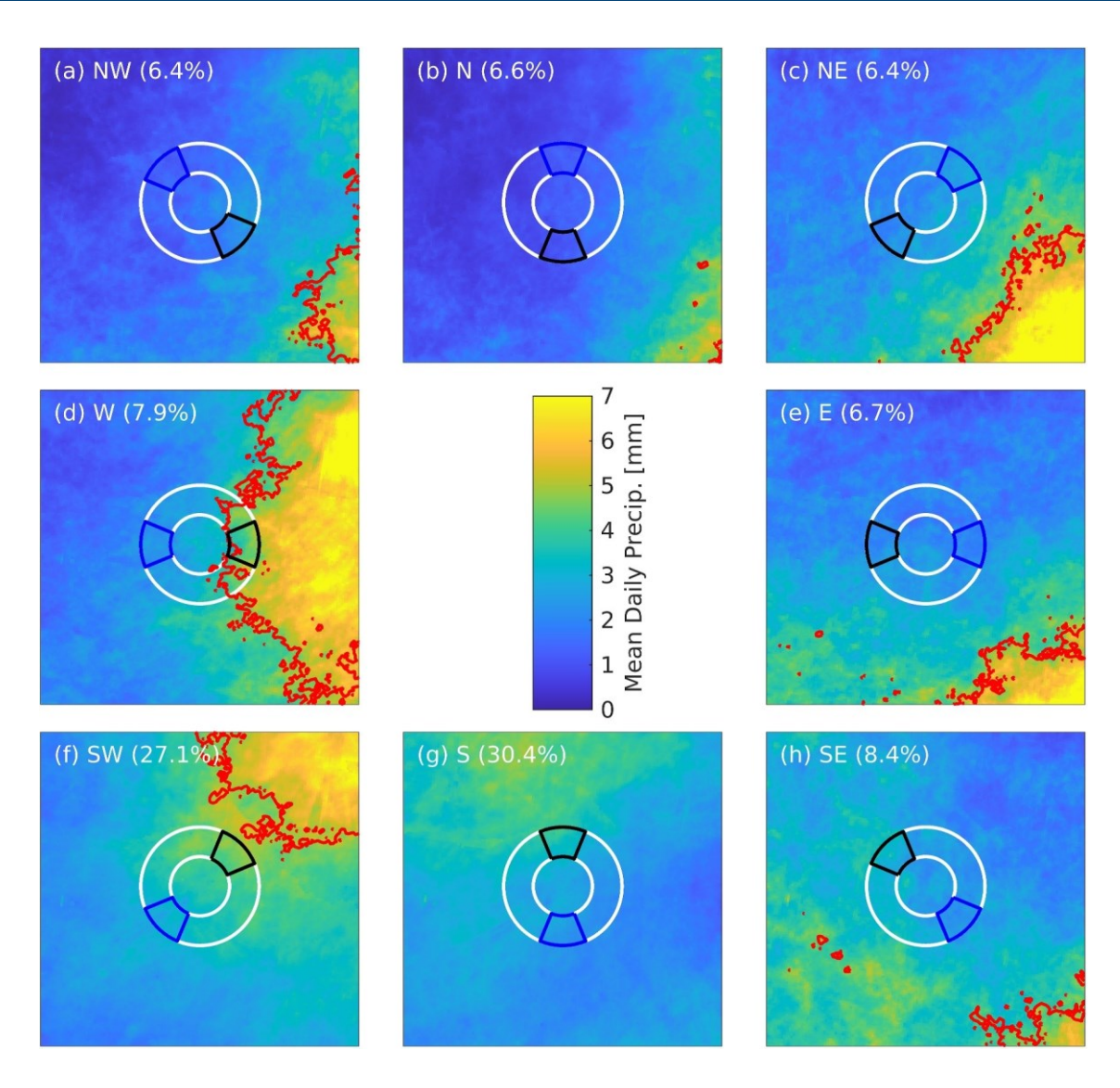


Figure 2. Mean daily precipitation during the warm season (MAMMJAS) of 2002–2021 in d03 (areal extent as shown in Figures 1b and 1c) from Stage IV, conditionally sampled by 850 hPa wind direction from ERA5. Numbers denote the frequency of observations in each directional sector. White rings show 50 and 100-km radii around the centroid of DFW. Wind-direction-specific sub-sampling areas for quantitative comparison of precipitation upwind (blue outline) and downwind (black outline) of DFW are shown in each panel. Red contours denote areas where >20% of days have daily precipitation >5 mm.

 Table 1

 Total Number of Days With Statistically Different Mean Rainfall Totals in Annulus Sectors Upwind (UW) and Downwind (DW) of DFW (45° Sectors, 50–100 km From DFW) Based on a Wilcoxon Rank Sum Test

	$0 < R_{mean} < 1 \text{ mm}$	1< R <sub>mean</sub> <6 mm	R <sub>mean</sub> > 6 mm	$R_{mean}$ > 6 mm and MMD < 100 km	$R_{mean}$ > 6 mm and MMD > 100 km
Total sample size	864	424	429	331	98
UW significantly higher	274	177	227	188	39
DW significantly higher	407	198	158	110	48

*Note.* Results are reported for three precipitation classes defined based on the mean of RR in all Stage IV grid cells in the upwind sector ( $R_{mean}$ ). The class  $0 < R_{mean} < 1$  mm includes 50% of all days with precipitation in both the UW and DW sectors, the other two  $R_{mean}$  classes contain 25% of the data each. The rightmost two columns contain the results when the  $R_{mean} > 6$  mm class is conditionally sampled be mean minimum distance (MMD) as a metric for the spatial scale of precipitation events.

ZHOU ET AL. 8 of 22

21698996, 2024, 10, Downloaded from https://agupubs.onlinelibrary.wiley.com/doi/10.1029/2023JD039972 by Comell University Library, Wiley Online Library on [29/07/2024]. See the Terms and Conditions (https://onlinelibrary.wiley.com/terms

and-conditions) on Wiley Online Library for rules of use; OA article

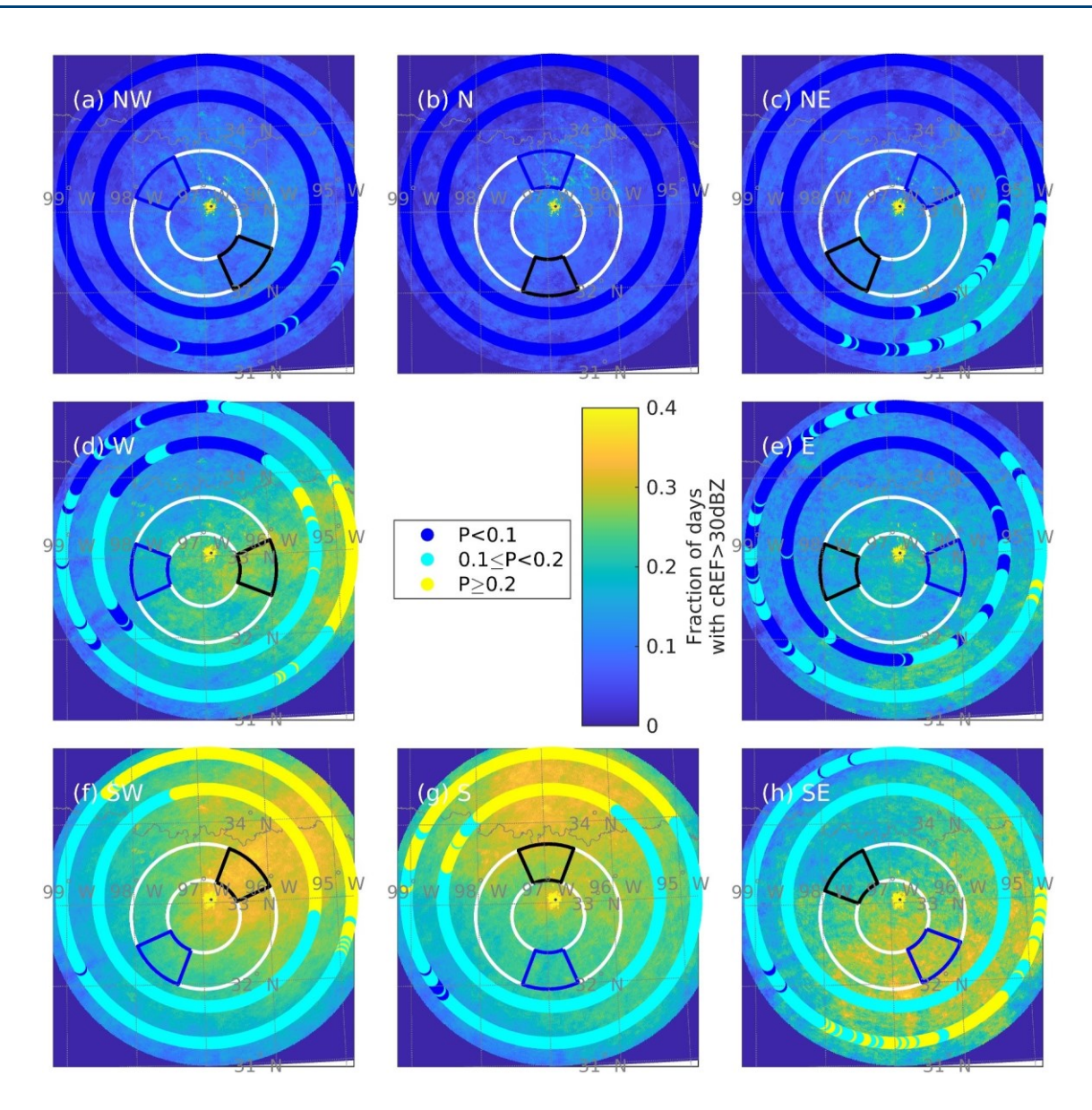


Figure 3. Frequency of occurrence of daily maximum cREF >30 dBZ in MAMJJAS of 2014–2021, conditionally sampled by 850 hPa wind direction. Colored rings show the probability of occurrence in three classes of daily hail or graupel signature at 150 and 200 km from the KFWS RADAR station. White rings show 50 and 100km radii around the centroid of DFW. Wind-direction-specific sub-sampling areas for quantitative comparison of cREF upwind (blue outline) and downwind (black outline) of DFW are shown in each panel.

hail or graupel being reported by the RADAR HCC for westerly, southwesterly and southerly flow is >20% at both 150 and 200 km downwind of the KFWS RADAR station while upwind hail and graupel probabilities are between 10% and 20%. Hail and graupel are much less common for locations not downwind of DFW, with the exception of southeasterly flow, when higher cREF and hail/graupel HHC reports are more frequent upwind (south and east) of the urban area (Figure 3).

The effect of the city on cloud top heights is much less evident. Daily maximum CTH >10,000 geopotential meters (gpm) are more frequent downwind of DFW than upwind of the city under northerly (47% higher probability in the DW sector) and westerly flow (41% higher probability in the DW sector), while all other wind directions are associated with a lower frequency of occurrence of CTH >10,000 gpm in the downwind sector (lower by 3%—

ZHOU ET AL. 9 of 22

Library, Wiley Online Library on [29/07/2024]. See the



20% than in the upwind sector). RADAR-tracked storm cells also show an increased frequency of high CTH downwind of DFW under westerly flow (SI Figure S3 in Supporting Information S1).

It is important to acknowledge the presence of regional scale gradients in the SGP hydroclimate. For example, total accumulated warm season precipitation from Stage IV grid cells in the eastern third of domain d03 are ~40% higher than those in the western third. This may be the root-cause of urban rainfall enhancement effects beyond a 200-km range downwind under some flow conditions (Figure 2). These regional gradients likely arise due to the increased proximity to the Gulf of Mexico under northwesterly flow and the increased terrain elevation to the north of DFW (Figure 1a). It is difficult to de-convolve these effects from observations alone and is the reason that the workflow used herein also includes numerical simulations. Nevertheless, the synthesis of these analyses is that the upper tail of the probability distribution of rainfall rates in the downwind sector is generally extended relative to the upwind sector. However, for events with very heavy precipitation upwind of the city the spatially averaged mean daily rainfall downwind is generally lower than the upwind value. This may imply that the urban surface differentially affects different types of precipitation events (Schmid & Niyogi, 2017) and may suppress precipitation in some parts of an MCS while enhancing other parts of the system (X Chen et al., 2023). Analyses of two events with heavy precipitation, that is, that fall within the precipitation class where observations indicate relative suppression of precipitation in the downwind sector, are reported below using simulations with WRF.

## 4. WRF Simulations of Deep Convection Events

### 4.1. Control Simulations

All CTL simulations capture the broad geospatial structure of precipitation and cREF during the two MCS events. Nevertheless, there are marked differences in 24-hr precipitation totals ( $t_p \pm 12$  hr) and cREF across the five different configurations (Figure 4) and variation in terms of fidelity relative to RADAR observations (Figures 4a–4d). Differences between the WRF ensemble members are more marked for the more locally forced and less spatially extensive event. Indeed, for the July event only the MILB and MORR schemes capture the spatial extent of high cREF and the propagation of the MCS over DFW (Figure 4h,I). In the July event, MORR and MILB schemes also produce the highest spatial coverage of cREF >30 dBZ. The extent of cREF >30 dBZ is 1.2 (MORR) and 0.7 (MILB) times that of RADAR observations. The spatial overlap with the observed high cREF is 54% and 24% from MORR and MILB, respectively. The WRF simulations also overestimate the precipitation totals in the July case. For example, the simulated areal extent with 24-hr precipitation >40 mm is a factor of 10

more spatially extensive than the estimated from RADAR (Figure 4). For the March event, all simulations exhibit an areal overlap of >37% with observed cREF >30 dBZ and all have a >67% areal overlap with observations for regions with 24-hr precipitation above 40 mm. The microphysical schemes with the best areal agreement with RADAR in terms of heavy precipitation and cREF >30 dBZ during the March case are MILB (87% areal overlap for cREF, 78% for precipitation) and MORR (78% for cREF, 85% for precipitation).

For the March case, the time evolution of simulated spatially averaged RR exhibits relatively good agreement with the RADAR, although all ensemble members overestimate the peak RR by up to 30% close to passage of the MCS over DFW (at  $t_p$  in hour 19 to 20 of the simulation, Figure 5a). This leads to a positive bias in total accumulated precipitation within domain d03 (Figure 5b). RADAR within d03 indicates a spatially averaged total accumulated precipitation of 16 mm while the five WRF ensemble members yield values of 18–24 mm (Figure 5b). However, the spatial extent of RR > 4 mm/hr tends to be underestimated in the WRF simulations close to  $t_p$  particularly for the THOMA and WDM7 schemes (Figure 5g). Larger variations exist in cREF across different ensemble members due to the dependence of reflectivity on the sixth power of droplet diameter. Nevertheless, four out of the five ensemble members have a positive bias in the spatial extent of high cREF, the exception is WDM7 (Figure 5i). Simulations of the July case also exhibit a positive bias in terms of total accumulated precipitation (Figure 5d) and the spatial occurrence of hail and graupel except for MORR (Figure 5l). The WRF

ZHOU ET AL. 10 of 22



simulations also generate two distinct periods with heavy precipitation rather than the single moreprolonged period as is evident in RADAR observations (Figure 5b).

There is generally a positive association between the domain d03 spatial coverage of high rainfall rates (RR > 4 mm/hr), high cREF (cREF >30 dBZ) and high CTH (CTH >10 km) through time in all simulations (Figure 6). However, the degree of association is highly variable across the microphysical schemes and time histories of these properties are markedly divergent (Figure 6). Simulations with both the MILB and MORR schemes exhibit clear bifurcation in the relationship between the spatial coverage of RR and cREF before and after the system's passage over DFW in the March case (Figures 6a–6e). That is before the MCS crosses DFW there is a clear positive slope in the relationship between these properties while afterward the slope of this

ZHOU ET AL. 11 of 22

2169896, 2024, 10, Downloaded from https://agupubs.onlinelibrary.wiley.com/doi/10.1029/2023ID039972 by Comell University Library. Wiley Online Library on [29 07/2024]. See the Terms and Conditions (https://onlinelibrary.wiley.com/emms-ad-conditions) on Wiley Online Library for rules of use; OA articles are governed by the applicable Certaive Commons License

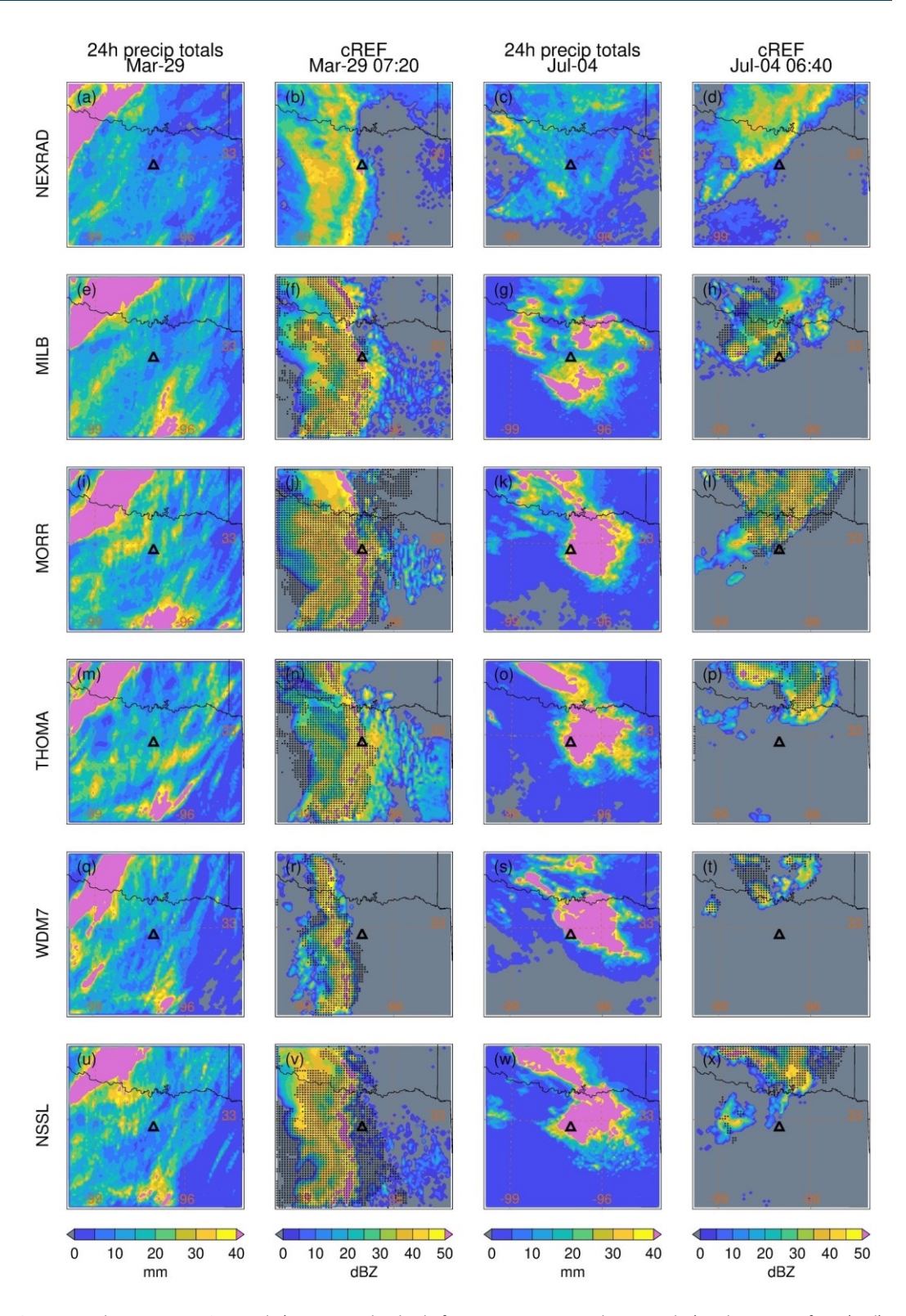


**Figure 4.** 24-hour precipitation totals (20:00 UTC the day before to 20:00 UTC on the event day) and cREF at  $t_p$  from (a–d) RADAR and simulated using WRF with (e–h) MILB (i–l) MORR (m–p) THOMA (c–t) WDM7 (u–x) NSSL microphysical schemes. Frames of cREF also show the MCS mask (shading). The triangle denotes the DFW centroid.

ZHOU ET AL. 12 of 22

21698996, 2024, 10, Downloaded from https://agupubs.onlinelibrary.wiley.com/doi/10.1029/2023JD039972 by Cornell University Library, Wiley Online Library on [29/07/2024]. See the Terms and Conditions (https://onlinelibrary.wiley.com/terms-and-conditions) on Wiley Online Library for rules of use; OA articles are

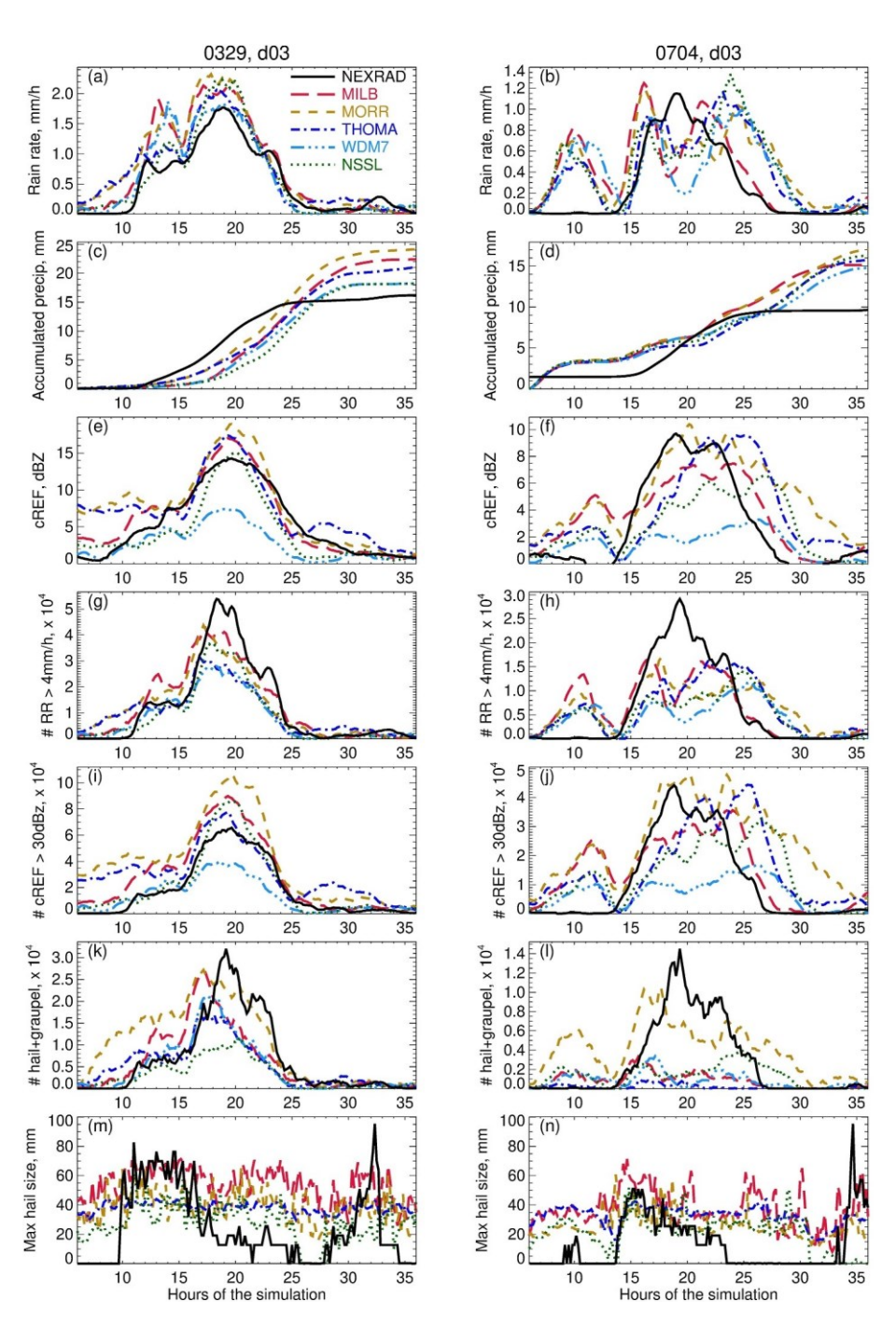


Figure 5. Domain d03 wide (a–b) mean rain rate (RR, mm/h) (c–d) 24-hr accumulated precipitation (mm) (e–f) mean cREF (dBZ), number of grids with (g–h) RR > 4 mm/hr (i–j) cREF >30 dBZ (k–l) hail and graupel (m–n) maximum hail size for the 29 March (left) and 4 July (right) events simulated using the different microphysical schemes. Note that the max hail size is not available from the WDM7 scheme in WRF v4.3. In both cases, the deep convection passed over DFW during the nineteenth - twentieth hour of the simulation.

association is much shallower indicating that while the areal extent of cREF >30 dBZ remained high, the spatial coverage of RR > 4 mm/hr markedly decreased. Similar bifurcation is also evident in the association between spatial coverage of high cREF and high CTH, with large spatial coverage of high CTH remaining after the passage over DFW while the spatial extent of high cREF declines more rapidly (e.g., Figure 6f). The relationship between

ZHOU ET AL. 13 of 22

0.0

**Figure 6.** Time histories of the co-occurrence between convective cores in terms of spatial coverage of high RR (>4 mm/hr), cREF (>30 dBZ), and CTH (>10 km) based on simulations with (a–d) MILB (e–h) MORR (i–l) THOMA (m–p) WDM7, and (c–t) NSSL. First-second columns show 0329 case, and third-fourth columns show 0704 case. Points are colored by the time in the simulation and the time when convections passed over DFW, t<sub>p</sub>, in each simulation is denoted by the triangle.

1029/2023JD039972 by Cornell University Library, Wiley Online Library

on [29/07/2024]

of multiple convective systems in the simulations, but the relationships are consistent with the March case in that after passage over DFW while the spatial coverage of high RR and cREF tend to decline rapidly, the areal extent with high CTH remains relatively large.

In general, the spatiotemporal samples of storm-related properties during the 24-hr period (centered at the twentieth hour of simulation) show better model performance in the March case than in the July case. Among the microphysical schemes, MILB and MORR have the best overall performance based on the evaluation metrics (Supplementary Section 1 and Table S1 in Supporting Information S1), especially over a period close to the passage of system over the city. Therefore, we use model configurations with MILB and MORR in the assessment of urban influence and in the perturbation experiments.

### 4.2. Perturbation Experiments

For the March case, all DFW  $\times$  0 simulations exhibit a decrease in RR, updraft velocity, and mean cREF within the MCS region as the system moves over the location of DFW. The means of those properties in the MCS region one hour after the system passed over the location of DFW are lower than in the one-hour prior (Table 2). Thus, in the absence of the city, the system was weakening as it transited over the DFW location. Mean RR in the MCS was approximately 50% lower in the downwind region in this perturbation experiment (Table 2). For some of the land use perturbation experiments with the city present and expanded, this tendency is partly reversed. However, the influence of DFW on precipitating areas of deep convection (i.e., MCS with cREF >20 dBZ) is non-linearly related to the size of the DFW urban area and is a strong function of the microphysical scheme. For the March case, increased urban expanse generally results in small reductions of the mean downwind RR in simulations using MILB. Conversely, simulations with MORR generally indicate an increase in downwind RR as urban extent increases, though the increase in RR downwind because of the urban area is of smaller magnitude than the decline in the DFW  $\times$  0 case over time. Thus, even an 8-fold expansion of the city is insufficient to overcome the inherent weakening in DFW  $\times$  0. The urban expansion experiments with MILB and MORR both show a decrease in the spatial extent of cREF >20 dBZ in the downwind sector under the MCS, and also a reduction in updraft velocities.

The DFW  $\times$  0 simulation of the July event implies the MCS was slightly (MILB) or strongly (MORR) strengthening as it moved over DFW leading to higher RR downwind of the DFW location. All urban perturbation experiments performed with MORR indicate a reduction in MCS-related RR downwind of the city relative to the DFW  $\times$  0 simulation (Table 2). However, as with the March case, the responses are non-linearly related to the size of DFW and differ between the two microphysical schemes. It is noteworthy that overall responses of MCS

<b>Table 2</b> Urban Influence on MCS Pro	Table 2 Urban Influence on MCS Properties Downwind (DW) and Upwind (UW) of DFW							
1h DW – 1h UW 0329	DFW × 0	DFW × 1 (CTL)-DFW × 0	DFW × 2-DFW × 0	DFW × 4-DFW × 0	DFW × 8-DFW × 0			

ZHOU ET AL. 14 of 22



# Journal of Geophysical Research: Atmospheres

10.1029/2023JD039972

RR, mm/h MILB		- 3.02 (- 48.5%)	- 0.02 (- 0.4%)	0.15 (2.4%)	- 0.16 (- 2.6%)	- 0.20 (- 3.2%)
	MORR	- 3.37 (- 58.7%)	0.06 (1.0%)	0.37 (6.4%)	0.32 (5.5%)	0.28 (4.9%)
cREF, dBZ	REF, dBZ MILB - 3.07 (- 8.0%) MORR - 3.43 (- 8.7%)		- 0.51 (- 1.3%)	- 0.82 (- 2.1%)	- 0.71 (- 1.9%)	- 0.98 (- 2.5%)
			- 0.11 (- 0.3%)	- 0.03 (- 0.1%)	- 0.17 (- 0.4%)	- 0.07 (- 0.2%)
Updraft, m/s	MILB	- 0.75 (- 25.2%)	- 0.92 (- 30.8%)	- 0.79 (- 26.5%)	- 0.85 (- 28.3%)	- 0.74 (- 24.8%)
	MORR	- 1.52 (- 46.7%)	- 1.52 (- 46.7%)		- 0.05 (- 1.4%)	- 0.05 (- 1.4%)
1h DW – 1h UV	V 0704	DFW × 0	DFW × 1 (CTL)-DFW × 0	DFW × 2-DFW × 0	DFW × 4-DFW × 0	DFW × 8-DFW × 0
RR, mm/h	MILB	0.81 (14.8%)	1.55 (28.1%)	- 1.05 (- 18.9%)	- 0.09 (- 1.6%)	0.12 (2.2%)
	MORR	4.79 (79.2%)	- 2.01 (- 33.3%)	- 0.24 (- 4.0%)	- 1.66 (- 27.4%)	- 2.34 (- 38.7%)
cREF, dBZ	MILB	- 1.30 (- 3.5%)	2.91 (7.8%)	0.57 (1.5%)	0.65 (1.8%)	1.39 (3.7%)
	MORR	4.90 (12.7%)	- 3.86 (- 10.0%)	0.05 (0.1%)	1.30 (3.4%)	0.68 (1.8%)
Updraft, ı	m/s	MILB - 0.79 (- 1		0.04 (1.0%) 0.86 (- 25.6%) 0.19 (5.0%)	5 (21.0%) 0.42 (1 0.65 (17.3%)	0.2%) MORR 1.40 0.51 (13.6%)

Note. Properties are averaged over the MCS grids with cREF >20 dBZ in a 200  $\times$  200 km box centered on DFW during the hour prior to MCS passage (upwind, UW) and 1 hr subsequent thereto (downwind, DW). Values in the DFW  $\times$  0 column indicate the difference in mean RR, cREF, and updraft velocity in the MCS region sampled DW and UW of the DFW location and thus represent the MCS natural evolution. Negative values indicate lower values DW. Other columns show the difference in value DW and UW from the DFW  $\times$  Y (Y = 1,2,4,8) minus the reference (DFW  $\times$  0). Thus, positive values indicate that the difference in mean value DW minus UW is LARGER in the land use perturbation experiment. The corresponding percentage changes relative to the spatiotemporally averaged MCS-scale properties during the period of  $t_0 \pm 1h$  in CTL run are shown in the paratheses.

properties in July case are larger and opposite to the March case indicating the complex nature of urban effect on existing MCSs and the importance of the large-scale forcing.

The probability distributions of properties sampled in time ( $\pm 1.5$  hr from  $t_p$ ) and space (over  $300 \times 300$  km subdomain centered on DFW) and thus over both the MCS and surrounding areas indicate much clearer impacts from urban extent in the July case (Figure 7) than the March case (SI Figure S4 in Supporting Information S1). Generally increased urban extent with the MORR scheme reduces RR (Figure 7b) across all values above approximately 6 mm/hr consistent with the observational analyses (Table 1). For this microphysical scheme, urban expansion also reduces the probability of large-magnitude updrafts (Figure 7d), downdrafts (Figure 7f) and hail (Figure 7n). The converse is generally found for MILB, where the 8 × DFW perturbation experiment leads to enhancement of RR, updraft velocities, liquid water path, and hail and graupel production (Figures 7a–7c and 7i, 7m).

Although the signs of responses to urbanization are divergent across simulations with the two microphysical schemes, they are internally consistent with physical expectations in terms of feedbacks from cloud microphysics to storm dynamics through diabatic heating and cooling (Hugh Morrison & Milbrandt, 2014; Morrison et al., 2014). With increased size of DFW, MILB simulations generate larger condensation and hence liquid water path (LWP) (Figure 7i) plus latent heat release in the updraft region. The smaller raindrop radii lead to enhanced evaporative cooling and hence downdraft intensity. Note that MILB scheme generates slightly larger Nc and smaller cloud droplets with larger urban extent. The smaller cloud droplets result in less efficient auto-conversion and growth of raindrops; therefore, more condensed water stays within the cloud. In comparison, MORR produces lower LWP and thus relatively small latent heat release in simulations with a larger urban area, leading to weaker updrafts (Figure 7). MORR generates larger raindrops which leads to smaller evaporative cooling and weaker downdrafts in simulations when DFW is expanded. The negative dynamic feedback to expanded urban areas implied in the simulations with MORR may be related to the use of a singlemoment description of cloud droplets. Although Nc is fixed in MORR scheme, the mean cloud droplet radius is slightly larger with larger urban extent, which results in more efficient auto-conversion and growth of raindrops, and thus opposite responses of MCSs to urban extent than in simulations with MILB. As described above, urban impacts on rainfall rates have been shown to exhibit a sensitivity to the regional aerosol burden. Although this

ZHOU ET AL. 15 of 22

2169896, 2024, 10. Downloaded from https://agupubs.onlinelibrary.wiley.com/doi/10.1029/2023JD039972 by Cornell University Library, Wiley Online Library, wiley.com/terms-and-conditions) on Wiley Online Library for rules of use; OA articles are governed by the applicable Creative Commons Licenses and Conditions (https://onlinelibrary.wiley.com/terms-and-conditions) on Wiley Online Library for rules of use; OA articles are governed by the applicable Creative Commons Licenses

is not the primary focus of this study, the different realizations of Nc in MILB and MORR schemes inherently include the aerosol effect.

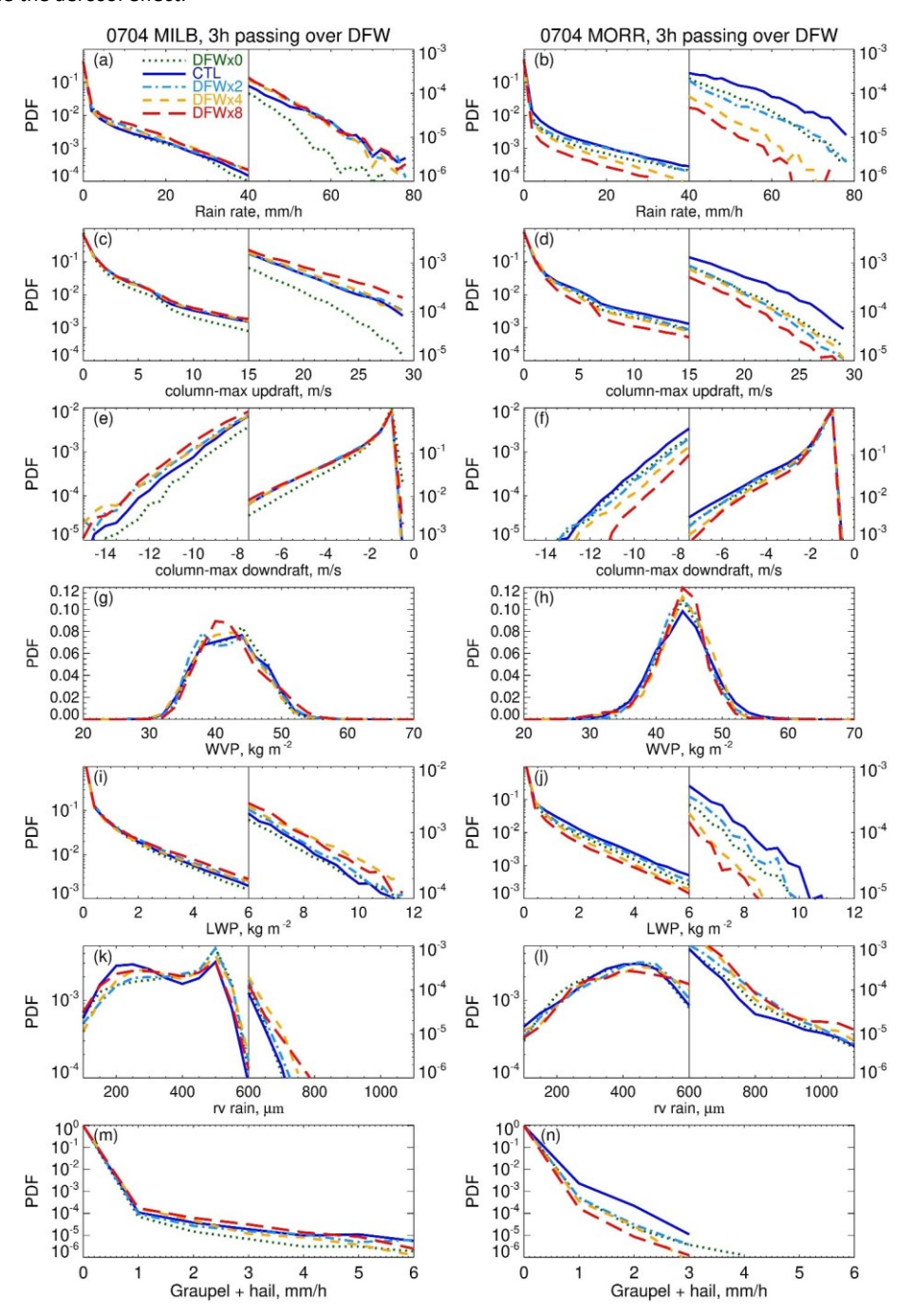


Figure 7. Probability distributions of (a–b) rain rate (c–d) maximum updraft in the column (e–f) maximum downdraft in the column (g–h) water vapor path (WVP) (i–j) liquid water path (LWP) (k–l) volume mean radius of rain drops (m–n) hail and graupel derived by sampling WRF output every 10-min during the period within  $t_p \pm 1.5$  hr and all grid cells within a 300 km by 300 km sub-domain centered on DFW. Simulations of the 4 July case using MILB (left) and MORR (right) for the five different extents of DFW.

ZHOU ET AL. 16 of 22

ned by the applicable Creative Commons License

Simulations of the 4 July case with a higher prescribed Nc of 350 cm<sup>-3</sup> exhibit the same change of sign as those from simulations performed with Nc set to 250 cm<sup>-3</sup> (Figure S5 in Supporting Information S1). Thus, the differences in simulated response to urban expansion for MORR and MILB do not appear to be solely the result of the inconsistent Nc in the two schemes.

## 5. Concluding Remarks

Urban impacts on the local and regional hydroclimate derive from changes in the surface energy balance, roughness length and aerosol effects. Although most prior research has indicated downwind enhancement of precipitation, the actual impact varies across individual events, cities, and environmental contexts. Here we present a blended analysis of long-term observations and WRF perturbation experiments centered on the DallasFort Worth (DFW) area.

Long-term records from Stage IV, RADAR and GOES-16 satellite observations, indicate clear evidence that for flow from the south, southwest and west there is downwind enhancement of daily total precipitation, hail occurrence, compositive reflectivity >30 dBZ and the probability of cloud top heights above 10,000 gpm. However, the downwind distance at which these properties are enhanced varies according to the property under consideration and no statistically significant downwind enhancement is found for other wind directions, possibly due to the presence of other causes of spatial variability in regional hydroclimate (e.g., orography and proximity to the Gulf coast). Nevertheless, daily precipitation, in a randomly drawn downwind grid cell from an annulus sector with an azimuth width of 45-degree at 50–100 km, is a factor of 1.4 higher than comparable upwind values on the median precipitation day. Higher percentile values (i.e., the precipitation in the wettest grid cells) exhibit slightly greater downwind enhancement. However, mean precipitation totals are significantly lower downwind on the upper quartile of rainfall days (i.e., when the spatial mean daily precipitation >6 mm). Additionally, the influence of the city on downwind precipitation exhibits a clear dependence on the spatial scale of forcing. To examine this effect in more detail, 2 days with deep convection and high daily rainfall totals (>6 mm) are subject to simulations with WRF using a range of microphysics parameterizations.

WRF simulations with all five microphysical schemes (MILB, MORR, THOMA, WDM7, NSSL) capture most aspects of the event with stronger large-scale forcing but several exhibit poorer performances for a more locally forced event. Simulations with Milbrandt-Yau and Morrison generally exhibit the best agreement with observed cREF, precipitation amounts, hail and graupel. Thus, perturbation experiments are conducted using these two microphysical schemes wherein the areal extent of urban land cover is varied. In these experiments the DFW urban area is replaced by grassland and then DFW is expanded to twice, four-times and eight-times the current extent. The atmospheric impacts of these urban modifications exhibit a strong dependence on the microphysical scheme, and consistent with expectations are more pronounced for the event with weaker synoptic forcing. While the responses of the MCSs are internally consistent across the microphysical schemes, the responses in terms of downwind precipitation enhancement/reduction are of different signs. In simulations with Milbrandt-Yau expansion of DFW yields a higher probability of very heavy precipitation, more graupel and hail, and stronger updrafts, while the converse is true for simulations with Morrison using initial cloud droplet number concentrations of both 250 and 350 cm<sup>-3</sup>. These differences suggest that at least some fraction of the inconsistency across past land-use perturbation experiments may be due to the precise model configuration applied. Expansion of the number of case studies considered and application of this research framework to other urban areas is required to assess the degree to which these differences across microphysical schemes are robust. But these results imply extra caution is needed in conducting and interpreting numerical studies on the urban rainfall enhancement effect. There is a clear need for best-practice guidance regarding the selection of the microphysical scheme, and further improvement of the model physics may be needed to make the results more robust and suitable for applications to hazard reduction in the face of land cover and atmospheric changes (Wing et al., 2022).

ZHOU ET AL. 17 of 22



# **Data Availability Statement**

ERA5 reanalysis (European Centre for Medium-Range Weather Forecasts, 2019) and Stage IV precipitation data (Du, 2011) were obtained from the Research Data Archive at the National Center for Atmospheric Research (NCAR). NWS ASOS 5-min data (NOAA National Weather Service et al., 2005) and NEXRAD RADAR data (NOAA National Weather Service et al., 2016) were obtained from the National Centers for Environmental Information (NCEI) at the National Oceanic and Atmospheric Administration (NOAA). GOES-16 satellite products were obtained from the Comprehensive Large Array-data Stewardship System (CLASS) at NOAA (NOAA et al., 2017). WRF model version 4.3 used in this study (Skamarock et al., 2019) is available from NCAR's WRF-Model GitHub repository at https://github.com/wrf-model/WRF/releases/tag/v4.3. The HRRR analysis used for WRF model boundary and initial conditions was downloaded from the NOAA National Centers

ZHOU ET AL. 18 of 22



# **Journal of Geophysical Research: Atmospheres**

## Acknowledgments

This research is supported by the US National Aeronautics and Space Administration (80NSSC21K1489), the US Department of Energy: Office of Science (DE-SC0016438), and the US National Science Foundation (OAC2209711). All simulations were performed on the Discover cluster from the NASA Center for Climate Simulations. Additional computational resources are provided by the NSF Extreme Science and Engineering Discovery Environment (XSEDE2) (award TG-ATM170024). The meso-scale system tracking algorithm is provided by Gregory S. Elsaesser and Jingbo Wu from NASA Goddard Institute for Space Studies. The thoughtful comments of three reviewers and the editor are gratefully acknowledged.

for Environmental Prediction (NCEP) via Amazon Web Services (AWS) (NOAA National Centers for Environmental Prediction, 2014). The WRF model output generated and namelist used in this study are hosted by the authors through the Science Gateways of National Energy Research Scientific Computing Center (NERSC) at the US Department of Energy, available at

https://portal.nersc.gov/archive /home/x/xinz/www/DFW\_deep conv.

## References

Bae, S., Hong, S.-Y., & Tao, W.-K. (2018).

Development of a single-moment cloud microphysics scheme with prognostic hail for the weather research and forecasting (WRF) model. Asia-Pacific Journal of Atmospheric Sciences, 55(2), 233–245. https://doi.org/10.1007/s13143-0180066-3

Beck, H. E., Pan, M., Roy, T., Weedon, G. P., Pappenberger, F., Van Dijk, A. I., et al.

(2019). Daily evaluation of 26 precipitation datasets using

Stage-IV gauge-radar data for the CONUS. Hydrology and Earth System Sciences, 23(1), 207–224. https://doi.org/10.5194/hess-23-207-2019
Bornstein, R., & Lin, Q. (2000). Urban heat islands and summertime convective thunderstorms in Atlanta: Three case studies. Atmospheric Environment, 34(3), 507–516. https://doi.org/10.1016/s1352-2310(99)00374-x

Burian, S. J., & Shepherd, J. M. (2005). Effect of urbanization on the diurnal rainfall pattern in Houston. *Hydrological Processes: International Journal*, 19(5), 1089–1103. https://doi.org/10.1002/hyp.5647

Burke, J. D., & Shepherd, J. M. (2023). The urban lightning effect revealed with geostationary lightning mapper observations. *Geophysical Research Letters*, 50(6), e2022GL102272. https://doi.org/10.1029/2022GL102272

Chandrasekar, V., Keränen, R., Lim, S., & Moisseev, D. (2013). Recent advances in classification of observations from dual polarization weather radars. *Atmospheric Research*, 119, 97–111. https://doi.org/10.1016/j.atmosres.2011.08.014 Changnon, S. A. (Ed.) (2016)., *Metromex: A review and summary* (p. 181). Springer.

Changnon, S. A., Semonin, R. G., & Huff, F. (1976). A hypothesis for urban rainfall anomalies. *Journal of Applied Meteorology*, 15(6), 544–560. https://doi.org/10.1175/1520-0450(1976)015<0544:ahfura>2.0.co;2

Changnon Jr, S. A. (1968). The La Porte weather anomaly—Fact or fiction? *Bulletin of the American Meteorological Society*, 49(1), 4–11. https://doi.org/10.1175/1520-0477-49.1.4

Changnon Jr, S. A. (1980). More on the La Porte anomaly: A review. Bulletin of the American Meteorological Society, 61(7), 702–711. https://doi.org/10.1175/1520-0477(1980)061<0702:motlpa>2.0.co;2

Chen, F., & Dudhia, J. (2001). Coupling an advanced land surface-hydrology model with the Penn State-NCAR MM5 modeling system. Part I:

Model implementation and sensitivity. *Monthly Weather Review*, 129(4), 569–585. https://doi.org/10.1175/1520-0493(2001)129<0569:

CAALSHS 2.0.CO: 2

Chen, F., Mitchell, K., Schaake, J., Xue, Y., Pan, H.-L., Koren, V., et al. (1996). Modeling of land surface evaporation by four schemes and comparison with FIFE observations. *Journal of Geophysical Research*, 101(D3), 7251–7268. https://doi.org/10.1029/95JD02165

Chen, X., Leung, L. R., Gao, Y., Liu, Y., & Wigmosta, M. (2023). Sharpening of cold-season storms over the western United States. *Nature Climate Change*, 13(2), 167–173. https://doi.org/10.1038/s41558-022-01578-0

Clark, R. R. (1979). A hydrologic reanalysis of the La Porte anomaly. Bulletin of the American Meteorological Society, 60(5), 415–421. https://doi.org/10.1175/1520-0477(1979)060<0415:ahrotl>2.0.co;2

Crum, T. D., Saffle, R. E., & Wilson, J. W. (1998). An update on the NEXRAD program and future WSR-88D support to operations. Weather and Forecasting, 13(2), 253–262. https://doi.org/10.1175/1520-0434(1998)013<0253:auotnp>2.0.co;2

Debbage, N., & Shepherd, J. M. (2019). Urban influences on the spatiotemporal characteristics of Runoff and precipitation during the 2009 Atlanta flood. *Journal of Hydrometeorology*. 20(1), 3–21. https://doi.org/10.1175/JHM-D-18-0010.1

Dixon, P. G., & Mote, T. L. (2003). Patterns and causes of Atlanta's urban heat island–initiated precipitation. *Journal of Applied Meteorology*, 42(9), 1273–1284. https://doi.org/10.1175/1520-0450(2003)042<1273:pacoau>2.0.co;2

Dou, J., Wang, Y., Bornstein, R., & Miao, S. (2015). Observed spatial characteristics of Beijing urban climate impacts on summer thunderstorms. Journal of Applied Meteorology and Climatology, 54(1), 94–105. https://doi.org/10.1175/jamc-d-13-0355.1

Du, J. (2011). NCEP/EMC 4KM gridded data (GRIB) stage IV data. Version 1.0 [Dataset]. UCAR/NCAR - Earth Observing Laboratory. https://doi.org/10.5065/D6PG1QDD

Elsaesser, G. S., Roca, R., Fiolleau, T., Del Genio, A. D., & Wu, J. (2022). A simple model for tropical convective cloud shield area growth and decay rates informed by geostationary IR, GPM, and Aqua/AIRS satellite data. *Journal of Geophysical Research: Atmospheres*, 127(10), e2021JD035599. https://doi.org/10.1029/2021jd035599

European Centre for Medium-Range Weather Forecasts. (2019). ERA5 reanalysis (0.25 degree Latitude-Longitude grid). [Dataset]. Computational and Information Systems Laboratory. https://doi.org/10.5065/BH6N-5N20.Research data archive at the national center for atmospheric research

Fan, J., Han, B., Varble, A., Morrison, H., North, K., Kollias, P., et al. (2017). Cloud-resolving model intercomparison of an MC3E squall line case: Part I—Convective updrafts. *Journal of Geophysical Research: Atmospheres*, 122(17), 9351–9378. https://doi.org/10.1002/2017jd026622

Feng, Z., Houze, R. A., Jr., Leung, L. R., Song, F., Hardin, J. C., Wang, J., et al. (2019). Spatiotemporal characteristics and large-scale environments of mesoscale convective systems east of the Rocky Mountains. *Journal of Climate*, 32(21), 7303–7328. https://doi.org/10.1175/jcli-d-

Feng, Z., Leung, L. R., Liu, N., Wang, J., Houze, R. A., Jr., Li, J., et al. (2021). A global high-resolution mesoscale convective system database using satellite-derived cloud tops, surface precipitation, and tracking. *Journal of Geophysical Research: Atmospheres*, 126(8), e2020JD034202. https://doi.org/10.1029/2020jd034202

Fiolleau, T., & Roca, R. (2013). An algorithm for the detection and tracking of tropical mesoscale convective systems using infrared images from geostationary satellite. *IEEE Transactions on Geoscience and Remote Sensing*, *51*(7), 4302–4315. https://doi.org/10.1109/TGRS.2012. 2227762

Fritsch, J., Kane, R., & Chelius, C. (1986). The contribution of mesoscale convective weather systems to the warm-season precipitation in the United States. *Journal of Climate and Applied Meteorology*, 25(10), 1333–1345. https://doi.org/10.1175/1520-0450(1986)025<1333: tcomcw>2.0.co;2

Gao, J., & Bukovsky, M. S. (2023). Urban land patterns can moderate population exposures to climate extremes over the 21st century. *Nature Communications*, 14(1), 6536. https://doi.org/10.1038/s41467-023-42084-x

# **Journal of Geophysical Research: Atmospheres**

Gauthier, M. L., Petersen, W. A., Carey, L. D., & Christian, H. J., Jr. (2006). Relationship between cloud-to-ground lightning and precipitation ice mass: A radar study over Houston. *Geophysical Research Letters*, 33(20). https://doi.org/10.1029/2006gl027244

ZHOU ET AL. 19 of 22

oaded

on [29/07/2024].

- Grell, G. A., & Freitas, S. R. (2014). A scale and aerosol aware stochastic convective parameterization for weather and air quality modeling. Atmospheric Chemistry and Physics. 14(10), 5233–5250. https://doi.org/10.5194/acp-14-5233-2014
- Han, J.-Y., Baik, J.-J., & Lee, H. (2014). Urban impacts on precipitation. Asia-Pacific Journal of Atmospheric Sciences, 50(1), 17–30. https://doi.org/10.1007/s13143-014-0016-7
- Hand, L. M., & Shepherd, J. M. (2009). An investigation of warm-season spatial rainfall variability in Oklahoma City: possible linkages to urbanization and prevailing wind. *Journal of Applied Meteorology and Climatology*, 48(2), 251–269. https://doi.org/10.1175/ 2008JAMC2036.1
- Heidinger, A. K., Pavolonis, M. J., Calvert, C., Hoffman, J., Nebuda, S., Straka III, W., et al. (2020). ABI cloud products from the GOES-R series, in *The GOES-R series*, edited, (pp. 43–62). Elsevier.
- Hersbach, H., Bell, B., Berrisford, P., Hirahara, S., Horányi, A., Muñoz-Sabater, J., et al. (2020). The ERA5 global reanalysis. Quarterly Journal of the Royal Meteorological Society, 146(730), 1999–2049. https://doi.org/10.1002/qi.3803
- Holzman, B., & Thom, H. (1970). The la Porte precipitation anomaly. Bulletin of the American Meteorological Society, 51(4), 335–337.
- Hu, H. (2015). Spatiotemporal characteristics of rainstorm-induced hazards modified by urbanization in Beijing. *Journal of Applied Meteorology and Climatology*, 54(7), 1496–1509. https://doi.org/10.1175/JAMC-D-14-0267.1
- Huff, F. A., & Changnon, S. A., Jr. (1973). Precipitation modification by major urban areas. Bulletin of the American Meteorological Society, 54(12), 1220–1233. https://doi.org/10.1175/1520-0477(1973)054<1220:Pmbmua>2.0.Co;2
- lacono, M. J., Delamere, J. S., Mlawer, E. J., Shephard, M. W., Clough, S. A., & Collins, W. D. (2008). Radiative forcing by long-lived greenhouse gases: Calculations with the AER radiative transfer models. *Journal of Geophysical Research*, 113(D13), D13103. https://doi.org/10.1029/2008/D009944
- Keuser, A. P. (2014). Precipitation patterns and trends in the metropolitan area of Milwaukee, Wisconsin. *International Journal of Geospatial and Environmental Research*. 1(1), 6.
- Khlopenkov, K. V., Bedka, K. M., Cooney, J. W., & Itterly, K. (2021). Recent advances in detection of overshooting cloud tops from longwave infrared satellite imagery. *Journal of Geophysical Research: Atmospheres*, 126(14), e2020JD034359. https://doi.org/10.1029/2020jd034359
- Kusaka, H., Nawata, K., Suzuki-Parker, A., Takane, Y., & Furuhashi, N. (2014). Mechanism of precipitation increase with urbanization in Tokyo as revealed by ensemble climate simulations. *Journal of Applied Meteorology and Climatology*, 53(4), 824–839. https://doi.org/10.1175/ JAMC-D-13-065.1
- Lauer, A., Pausata, F. S. R., Leroyer, S., & Argueso, D. (2023). Effect of urban heat island mitigation strategies on precipitation and temperature in Montreal, Canada: Case studies. *PLOS Climate*, 2(6), e0000196. https://doi.org/10.1371/journal.pclm.0000196
- Li, Y., Wang, W., Chang, M., & Wang, X. (2021). Impacts of urbanization on extreme precipitation in the Guangdong-Hong Kong-Macau greater Bay area. *Urban Climate*, 38, 100904. https://doi.org/10.1016/j.uclim.2021.100904
- Lin, Y., Fan, J., Jeong, J.-H., Zhang, Y., Homeyer, C. R., & Wang, J. (2021). Urbanization-induced land and aerosol impacts on storm propagation and hail characteristics. *Journal of the Atmospheric Sciences*, 78(3), 925–947. https://doi.org/10.1175/jas-d-20-0106.1
- Lin, Y., & Mitchell, K. E. (2005). 1.2 the NCEP stage II/IV hourly precipitation analyses: Development and applications. In *Paper presented at proceedings of the 19th conference hydrology*. American Meteorological Society. Citeseer.
- Liu, J., & Niyogi, D. (2019). Meta-analysis of urbanization impact on rainfall modification. Scientific Reports, 9(1), 7301. https://doi.org/10.1038/s41598-019-42494-2
- Mansell, E. R., Ziegler, C. L., & Bruning, E. C. (2010). Simulated electrification of a small thunderstorm with two-moment bulk microphysics. Journal of the Atmospheric Sciences, 67(1), 171–194. https://doi.org/10.1175/2009JAS2965.1
- Matyas, C. (2007). Quantifying the shapes of U.S. Landfalling tropical cyclone rain shields. The Professional Geographer, 59(2), 158–172. https://doi.org/10.1111/ji.1467-9272.2007.00604.x
- McLeod, J., & Shepherd, J. M. (2022). A synoptic framework for forecasting the urban rainfall effect using composite and K-means cluster analyses. Frontiers in Environmental Science, 10. https://doi.org/10.3389/fenvs.2022.808026
- McLeod, J., Shepherd, J. M., & Konrad, C. E. (2017). Spatio-temporal rainfall patterns around Atlanta, Georgia and possible relationships to urban land cover. *Urban Climate*, 21, 27–42. https://doi.org/10.1016/j.uclim.2017.03.004
- Milbrandt, J. A., & Yau, M. K. (2005). A multimoment Bulk microphysics parameterization. Part I: Analysis of the role of the spectral shape parameter. *Journal of the Atmospheric Sciences*, 62(9), 3051–3064. https://doi.org/10.1175/JAS3534.1
- Morrison, H., & Milbrandt, J. A. (2014). Parameterization of cloud microphysics based on the prediction of Bulk ice particle properties. Part I: Scheme description and idealized tests. *Journal of the Atmospheric Sciences*, 72(1), 287–311. https://doi.org/10.1175/JAS-D-14-0065.1
- Morrison, H., Milbrandt, J. A., Bryan, G. H., Ikeda, K., Tessendorf, S. A., & Thompson, G. (2014). Parameterization of cloud microphysics based on the prediction of Bulk ice particle properties. Part II: Case study comparisons with observations and other schemes. *Journal of the Atmospheric Sciences*, 72(1), 312–339. https://doi.org/10.1175/JAS-D-14-0066.1
- Morrison, H., Thompson, G., & Tatarskii, V. (2009). Impact of cloud microphysics on the development of trailing stratiform precipitation in a simulated squall line: Comparison of one- and two-moment schemes. *Monthly Weather Review*, 137(3), 991–1007. https://doi.org/10.1175/2008MWR2556.1
- Nadolski, V. (1998). Automated surface observing system (ASOS) user's guide. National Oceanic and Atmospheric Administration, Department of Defense, Federal Aviation Administration, 20.
- Nakanishi, M., & Niino, H. (2006). An improved Mellor–Yamada level-3 model: Its numerical stability and application to a regional prediction of advection Fog. Boundary-Layer Meteorology, 119(2), 397–407. https://doi.org/10.1007/s10546-005-9030-8
- Nelson, B. R., Prat, O. P., Seo, D.-J., & Habib, E. (2016). Assessment and implications of NCEP Stage IV quantitative precipitation estimates for product intercomparisons. Weather and Forecasting, 31(2), 371–394. https://doi.org/10.1175/waf-d-14-00112.1
- Niyogi, D., Lei, M., Kishtawal, C., Schmid, P., & Shepherd, J. M. (2017). Urbanization impacts on the summer heavy rainfall climatology over the eastern United States. *Earth Interactions*, 21(5), 1–17. https://doi.org/10.1175/ei-d-15-0045.1
- NOAA. (2016a). Federal meteorological handbook, No. 11 WSR-88D meteorologic observations Part A, system concepts, responsibilities, and procedures (p. 25). FCM-H11A-2016.
- NOAA. (2016b). Federal meteorological handbook, No. 11 WSR-88D meteorologic observations Part C, products and algorithms (p. 25). FCMH11A-2016
- NOAA (2017). WSR-88D meteorological observations: Part C WSR-88D products and algorithms. *Rep*, 394. FCM-H11C-2017, Silver Spring, MD. Retrieved from https://www.ofcm.gov/publications/fmh/FMH11/fmh11partC.pdf

ZHOU ET AL. 20 of 22

, 2024, 10, Downloaded from https

# **Journal of Geophysical Research: Atmospheres**

- NOAA National Weather Service, U.S. Federal Aviation Administration Air Force, U.S. (2016). Next generation weather radar (NEXRAD) [Dataset].

  NOAA National Centers for Environmental Information. Available online at: https://www.ncei.noaa.gov/products/radar/nextgeneration-weather-radar
- NOAA, NESDIS, & OSPO. (2017). GOES-R series ABI products (GRABIPRD) [Dataset]. Comprehensive Large Array-data Stewardship System. Retrieved from https://www.avl.class.noaa.gov/saa/products/search?datatype\_family=GRABIPRD
- NOAA National Centers for Environmental Prediction. (2014). NOAA high-resolution Rapid Refresh (HRRR) [Dataset]. NCEP, AWS. Retrieved from https://registry.opendata.aws/noaa-hrrr-pds/
- NOAA National Weather Service, U.S. Federal Aviation Administration, U.S. Department of Defense, and NOAA National Centers for Environmental Information. (2005). 5-Minute surface weather observations from the automated surface observing systems (ASOS) network, edited, NOAA national centers for environmental information. NCEI DSI 6401\_02. Available online at: https://data.noaa.gov/onestop/collections/ details/86e7ee1d-5451-4d58-898d-adb671df7b69
- Oke, T. R., Mills, G., Christen, A., & Voogt, J. A. (2017). Urban climates (p. 546). Cambridge University Press.
- Prein, A. F., & Holland, G. J. (2018). Global estimates of damaging hail hazard. Weather and Climate Extremes, 22, 10–23. https://doi.org/10.1016/i.wace.2018.10.004
- Pryor, S. C., Letson, F., Shepherd, T. J., & Barthelmie, R. J. (2023). Evaluation of WRF simulation of deep convection in the US southern Great Plains. *Journal of Applied Meteorology and Climatology*, 62(1), 41–62. https://doi.org/10.1175/jamc-d-22-0090.1
- Punge, H. J., & Kunz, M. (2016). Hail observations and hailstorm characteristics in europe: A review. Atmospheric Research, 176, 159–184. https://doi.org/10.1016/j.atmosres.2016.02.012
- Qian, Y., Chakraborty, T. C., Li, J., Li, D., He, C., Sarangi, C., et al. (2022). Urbanization impact on regional climate and extreme weather: Current understanding, uncertainties, and future research directions. *Advances in Atmospheric Sciences*, 39(6), 819–860. https://doi.org/10.1007/s00376-021-1371-9
- Rosenfeld, D., Lohmann, U., Raga, G. B., O'Dowd, C. D., Kulmala, M., Fuzzi, S., et al. (2008). Flood or drought: How do aerosols affect precipitation? Science, 321(5894), 1309–1313. https://doi.org/10.1126/science.1160606
- Rosenzweig, C., Solecki, W., Romero-Lankao, P., Mehrotra, S., Dhakal, S., & Ali Ibrahim, S. (Eds.) (2018)., Climate change and cities: Second assessment report of the urban climate change research network. Cambridge University Press. https://doi.org/10.1017/9781316563878
- Schmid, P. E., & Niyogi, D. (2017). Modeling urban precipitation modification by spatially heterogeneous aerosols. *Journal of Applied Meteorology and Climatology*, 56(8), 2141–2153. https://doi.org/10.1175/JAMC-D-16-0320.1
- Schmit, T. J., Gunshor, M. M., Menzel, W. P., Gurka, J. J., Li, J., & Bachmeier, A. S. (2005). Introducing the next-generation advanced baseline imager on GOES-R. Bulletin of the American Meteorological Society, 86(8), 1079–1096. https://doi.org/10.1175/bams-86-8-1079
- Seo, B.-C., Dolan, B., Krajewski, W. F., Rutledge, S. A., & Petersen, W. (2015). Comparison of single-and dual-polarization—based rainfall estimates using NEXRAD data for the NASA lowa Flood Studies project. *Journal of Hydrometeorology*, 16(4), 1658–1675. https://doi.org/10. 1175/jhm-
- Shem, W., & Shepherd, J. M. (2009). On the impact of urbanization on summertime thunderstorms in Atlanta: Two numerical model case studies. Atmospheric Research. 92(2), 172–189. https://doi.org/10.1016/j.atmosres.2008.09.013
- Shepherd, J. M., & Burian, S. J. (2003). Detection of urban-induced rainfall anomalies in a major coastal city. *Earth Interactions*, 7(4), 1–17. https://doi.org/10.1175/1087-3562(2003)007<0001:DOUIRA>2.0.CO:2
- Shepherd, J. M., Carter, M., Manyin, M., Messen, D., & Burian, S. (2010). The impact of urbanization on current and future coastal precipitation: A case study for Houston. Environment and Planning B: Planning and Design, 37(2), 284–304. https://doi.org/10.1068/b34102t
- Shepherd, J. M., Pierce, H., & Negri, A. J. (2002). Rainfall modification by major urban areas: Observations from spaceborne rain radar on the TRMM satellite. *Journal of Applied Meteorology*, 41(7), 689–701. https://doi.org/10.1175/1520-0450(2002)041<0689:RMBMUA>2.0.CO;2
- Skamarock, W. C., Klemp, J. B., Dudhia, J., Gill, D. O., Liu, Z., Berner, J., et al. (2019). A description of the advanced research WRF model version 4. National Center for Atmospheric Research
- Smalley, M., L'Ecuyer, T., Lebsock, M., & Haynes, J. (2014). A comparison of precipitation occurrence from the NCEP stage IV QPE product and the CloudSat cloud profiling radar. *Journal of Hydrometeorology*, 15(1), 444–458. https://doi.org/10.1175/jhm-d-13-048.1
- Stolz, D. C., Rutledge, S. A., & Pierce, J. R. (2015). Simultaneous influences of thermodynamics and aerosols on deep convection and lightning in the tropics. Journal of Geophysical Research: Atmospheres. 120(12), 6207–6231. https://doi.org/10.1002/2014jd023033
- Taylor, K. E. (2001). Summarizing multiple aspects of model performance in a single diagram. *Journal of Geophysical Research*, 106(D7), 7183–7192. https://doi.org/10.1029/2000JD900719
- Tewari, M., Chen, F., Wang, W., Dudhia, J., LeMone, M., Mitchell, K., et al. (2004). Implementation and verification of the unified NOAH land surface model in the WRF model, 20th conference on weather analysis and forecasting/16th conference on numerical weather prediction. Retrieved from https://ams.confex.com/ams/84Annual/techprogram/paper\_69061.htm
- Thompson, G., & Eidhammer, T. (2014). A study of aerosol impacts on clouds and precipitation development in a large Winter cyclone. *Journal of the Atmospheric Sciences*, 71(10), 3636–3658. https://doi.org/10.1175/JAS-D-13-0305.1
- Trapp, R. J., Hoogewind, K. A., & Lasher-Trapp, S. (2019). Future changes in hail occurrence in the United States determined through convectionpermitting dynamical downscaling. *Journal of Climate*, 32(17), 5493–5509. https://doi.org/10.1175/jcli-d-18-0740.1
- USGCRP. (2017). D. J. Wuebbles, D. W. Fahey, K. A. Hibbard, D. J. Dokken, B. C. Stewart (Eds.), Climate science special report: Fourth national climate assessment chapter 10: Changes in land cover and terrestrial biogeochemistry (p. 470). U.S. Global Change Research Program.
- Van Den Heever, S. C., & Cotton, W. R. (2007). Urban aerosol impacts on downwind convective storms. *Journal of Applied Meteorology and Climatology*, 46(6), 828–850. https://doi.org/10.1175/jam2492.1
- Wallace, R., Friedrich, K., Kalina, E. A., & Schlatter, P. (2019). Using operational radar to identify deep hail accumulations from thunderstorms. Weather and Forecasting, 34(1), 133–150. https://doi.org/10.1175/waf-d-18-0053.1
- Wang, J., Feng, J., & Yan, Z. (2018). Impact of extensive urbanization on summertime rainfall in the Beijing region and the role of local precipitation recycling. *Journal of Geophysical Research: Atmospheres*, 123(7), 3323–3340. https://doi.org/10.1002/2017jd027725 Wilks, D. S. (2011). *Statistical methods in the atmospheric sciences*. Academic press.

ZHOU ET AL. 21 of 22

21698996, 2024, 10, Downloaded from https

University Library, Wiley Online Library on [29/07/2024]. See the Terms and Conditions (https://onlinelibrary.wiley.com/terms-and-conditions) on Wiley Online Library for rules of use; OA articles are governed by the applicable Creative Commons License



- Wing, O. E. J., Lehman, W., Bates, P. D., Sampson, C. C., Quinn, N., Smith, A. M., et al. (2022). Inequitable patterns of US flood risk in the Anthropocene. *Nature Climate Change*, 12(2), 156–162. https://doi.org/10.1038/s41558-021-01265-6
- Witt, A., Eilts, M. D., Stumpf, G. J., Johnson, J., Mitchell, E. D. W., & Thomas, K. W. (1998). An enhanced hail detection algorithm for the WSR88D. Weather and Forecasting, 13(2), 286–303. https://doi.org/10.1175/1520-0434(1998)013<0286:aehdaf>2.0.co;2
- Wu, W., Liu, Y., & Betts, A. K. (2012). Observationally based evaluation of NWP reanalyses in modeling cloud properties over the Southern Great Plains. *Journal of Geophysical Research*, 117(D12). https://doi.org/10.1029/2011JD016971

# **Journal of Geophysical Research: Atmospheres**

- Xu, W., Rutledge, S. A., & Zhang, W. (2017). Relationships between total lightning, deep convection, and tropical cyclone intensity change. Journal of Geophysical Research: Atmospheres, 122(13), 7047–7063. https://doi.org/10.1002/2017jd027072
- Yeung, J. K., Smith, J. A., Baeck, M. L., & Villarini, G. (2015). Lagrangian analyses of rainfall structure and evolution for organized thunderstorm systems in the urban corridor of the northeastern United States. *Journal of Hydrometeorology*, *16*(4), 1575–1595. https://doi.org/10.1175/JHM-D-14-0095.1
- Yeung, J. K., Smith, J. A., Villarini, G., Ntelekos, A. A., Baeck, M. L., & Krajewski, W. F. (2011). Analyses of the warm season rainfall climatology of the northeastern US using regional climate model simulations and radar rainfall fields. *Advances in Water Resources*, 34(2), 184–204. https://doi.org/10.1016/j.advwatres.2010.10.005
- Yu, M., Miao, S., & Zhang, H. (2018). Uncertainties in the impact of urbanization on heavy rainfall: Case study of a rainfall event in Beijing on 7 August 2015. Journal of Geophysical Research: Atmospheres, 123(11), 6005–6021. https://doi.org/10.1029/2018jd028444
- Zhang, J., Zhou, Y.-s., & Shen, X.-y. (2020). Numerical simulation analysis of the impact of urbanization on an extreme precipitation event over Beijing–Tianjin–Hebei, China. *Atmosphere*, 11(9), 945. https://doi.org/10.3390/atmos11090945
- Zhang, Y., Smith, J. A., Luo, L., Wang, Z., & Baeck, M. L. (2014). Urbanization and rainfall variability in the Beijing metropolitan region. *Journal of Hydrometeorology*, 15(6), 2219–2235. https://doi.org/10.1175/JHM-D-13-0180.1
- Zhong, S., Qian, Y., Zhao, C., Leung, R., & Yang, X. Q. (2015). A case study of urbanization impact on summer precipitation in the Greater Beijing Metropolitan Area: Urban heat island versus aerosol effects. *Journal of Geophysical Research: Atmospheres*, 120(20), 903–910. https://doi.org/10.1002/2015jd023753914

ZHOU ET AL. 22 of 22